Wake redirection: comparison of analytical, numerical and experimental models

Wake redirection: comparison of analytical, numerical and experimental models

Jiangang Wang[1]**, Carlo L. Bottasso**[1,2]**, Filippo Campagnolo**[1]

[1] Wind Energy Institute, Technische Universität München, Boltzmannstraße 15, D-85748 Garching bei München, Germany
[2] Dipartimento di Scienze e Tecnologie Aerospaziali, Politecnico di Milano, Via La Masa 34, I-20156 Milano, Italy

E-mail: `jesse.wang@tum.de`

Abstract.
    This paper focuses on wake redirection techniques for wind farm control. Two control strategies are investigated: yaw misalignment and cyclic pitch control. First, analytical formulas are derived for both techniques, with the goal of providing a simple physical interpretation of the behavior of the two methods. Next, more realistic results are obtained by numerical simulations performed with CFD and by experiments conducted with scaled wind turbine models operating in a boundary layer wind tunnel. Comparing the analytical, numerical and experimental models allows for a cross-validation of the results and a better understanding of the two wake redirection techniques. Results indicate that yaw misalignment is more effective than cyclic pitch control in displacing the wake laterally, although the latter may have positive effects on wake recovery.

1. Introduction
Wake redirection is currently one of the most promising wind farm control methodologies, which might lead to improved power capture and reduced loading. In principle, wake redirection could be obtained in at least two different ways [8]: by intentionally misaligning the wind turbine with respect to the incoming wind (yaw misalignment, noted YM in the following), and by using a cyclically varying pitch input (cyclic pitch control, noted CyPC in the following). This paper uses a three-pronged approach to investigate these two techniques: analytical simplified models, whose goal is to provide the physical interpretation of the results, as well as higher-fidelity numerical and experimental techniques.

2. Methods
2.1. Simplified analytical model
The mathematical model was derived by establishing the correlation, for both control techniques, between a lateral force component at the rotor disk and a displacement of the wake in the same direction.

    A schematic view of a wind turbine is shown in Fig. 1. A ground-fixed frame of reference is noted XYZ, where the free stream wind is blowing along the X axis with a speed U_0. A nacelle-attached frame is noted xyz, rotated about the vertical axis z by the yaw misalignment angle φ. The rotor is spinning at an angular velocity Ω, while θ_i and ψ_i are, respectively, the

pitch and azimuthal angles of the ith of B blades. The tangential force acting locally at a generic blade section is noted F_t, while F_r is the radial component at that same location.
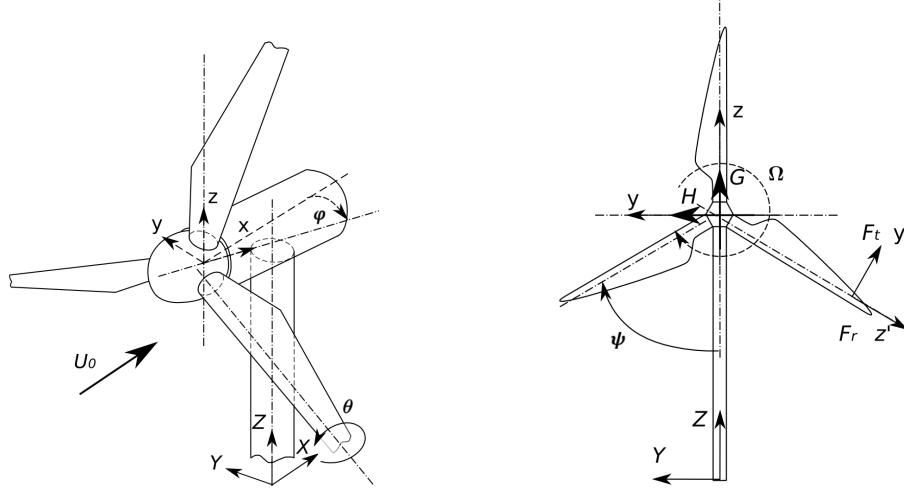

Figure 1: Coordinate frames and principal quantities for the wake displacement analytical models.

The velocity triangle at a generic blade section is shown on the left in Fig. 2, where U_T is the tangential velocity component, U_P the perpendicular one, ϕ is the inflow angle and α the angle of attack (AoA). Assuming a rigid rotor and small angles [14], the velocity components are readily found to be

$$U_P = U_0(1 - a), \tag{1a}$$
$$U_T = \Omega R(1 + a') - U_0 \varphi \cos(\psi_i), \tag{1b}$$

where a and a' are the axial and swirl inductions, respectively, and R the rotor radius. Both induction factors are assumed to be cyclically varying as

$$a = a_0 + a_s \sin(\psi_i + \gamma) + a_c \cos(\psi_i + \gamma), \tag{2a}$$
$$a' = a'_0 + a'_s \sin(\psi_i + \gamma) + a'_c \cos(\psi_i + \gamma). \tag{2b}$$

The cosine terms a_c and a'_c are induced by yaw misalignment or by cyclically pitching the blades with a phase angle γ. The sine terms a_s and a'_s account for the phase lag due to unsteady aerodynamics [1] caused by the cosine disturbances.

The right part of Fig. 2 shows the problem geometry as seen from above. The force resultants on the rotor are the thrust T and the in-plane force H, aligned with the nacelle-attached frame xyz. The resultant total aerodynamic force will in general have a non-zero component along the wind-orthogonal ground-fixed unit axis Y. By the principle of action and reaction, an equal and opposite force will be exerted by the rotor onto the air flow, resulting in a lateral displacement noted l at a distance X downstream from the wind turbine.

2.1.1. In-plane H force Looking at the left part of Fig. 2, the sectional tangential force is computed for a small inflow angle as $F_t = L\phi - D$, where L is the airfoil lift and D its drag. The lateral force H averaged over a rotor revolution is obtained as

$$H = \frac{1}{2\pi} \sum_{i=1}^{B} \int_0^{2\pi} \int_0^R (L\phi - D) \cos(\psi_i) \mathrm{d}\psi_i \mathrm{d}r, \tag{3}$$
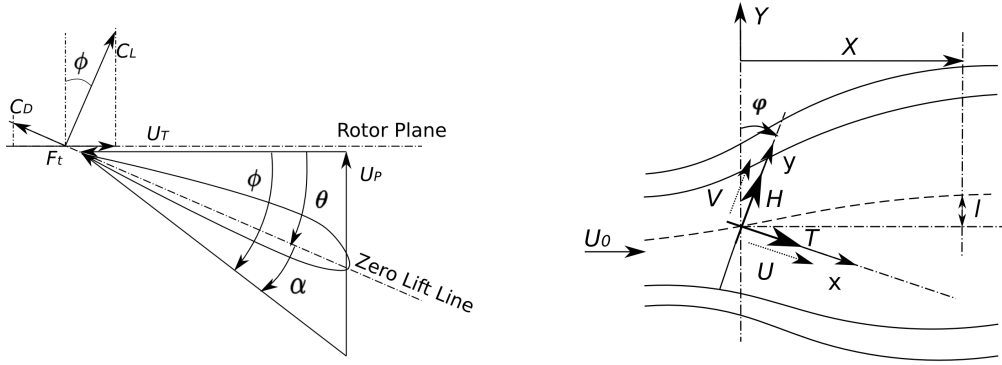
Figure 2: Left: velocity triangle at a generic blade section. Right: problem geometry as seen from above.

where the local lift $L = \frac{1}{2}\rho c C_{L\alpha}(U_P U_T - \theta U_T^2)$ and drag $D = \frac{1}{2}\rho c C_D U_T^2$ (per unit span) are expressed as functions of the tangential and perpendicular velocity components, while c is the chord, and the coefficients of lift and drag are $C_L = C_{L\alpha}\alpha$ and C_D, respectively.

Consider now the YM case, where in the partial load region $\theta \approx 0$, while the cyclic pitch phase is not relevant and therefore $\gamma = 0$. After simplification and assuming radially constant inductions, the expression for the in-plane force becomes

$$H_{\mathrm{YM}} = \frac{1}{4}\rho \hat{C}_D A U_0^2 \lambda \varphi - \frac{1}{2}\rho \hat{C}_L A U_0^2 a_c, \tag{4}$$

where A is the rotor area, $\lambda = \Omega R/U_0$ the tip speed ratio, $\hat{C}_D = C_D \sigma (1 + a_0')$ with σ indicating the rotor solidity, and $\hat{C}_L = C_{L\alpha}\sigma(1 - a_0)$. The first term in Eq. (4) is proportional to the yaw misalignment angle, while the second term is induced by cosine fluctuations of the axial induction (which are also assumed to be primarily caused by yaw misalignment, i.e. $a_c \approx a_{c\varphi}\varphi$).

In the CyPC case, the blade is pitched according to

$$\theta_i = \theta_0 + \theta_c \cos(\psi_i + \gamma), \tag{5}$$

where θ_0 is the collective pitch constant, θ_c the 1P pitch amplitude and γ is the phase angle. Assuming $\theta_0 \approx 0$ in the partial load region, the rotor in-plane force becomes

$$H_{\mathrm{CyPC}} = -\frac{1}{2}\rho \hat{C}_L A U_0^2 \lambda \left(\frac{2a_c}{\lambda} + \frac{1}{2}\theta_c\right) \cos(\gamma). \tag{6}$$

This expression shows that the rotor lateral force depends on the cyclic pitch amplitude and by the cosine fluctuations of axial induction caused by pitching (i.e. $a_c \approx a_{c\theta_c}\theta_c$).

2.1.2. Lateral wake displacement The lateral (i.e., orthogonal to the undisturbed wind) displacement of the wake is due to the presence of a lateral velocity component of the flow, caused by a corresponding lateral force component. The analysis can be carried in terms of forces, by using the thrust T and in-plane force H, or velocities, by using U and V. Although the two approaches clearly give the same result, the latter approach is preferred here, by relating V to the previously found expressions for H.

Noting V_Y as the lateral flow velocity along the Y direction at the rotor disk, the lateral wake displacement can be written as

$$\frac{l}{X} = C\frac{V_Y}{U_0}, \tag{7}$$

where C is a constant of proportionality. Velocity V_Y can be computed by assuming a small misalignment angle as

$$V_Y = V - U\varphi, \tag{8}$$

where $U = U_0(1 - a_0)$ (see the right part of Fig. 2). The rotor in-plane velocity V is readily obtained using the principle of impulse and momentum between the upstream section of the stream tube and a section immediately behind the rotor disk, as

$$H = (U_0\varphi - V)\dot{m}, \tag{9}$$

where $\dot{m}$ is the mass rate through the stream tube. By combining the previous expressions, one gets

$$\frac{V_{Y_{\text{YM}}}}{U_0} = \left(a_0 - \frac{\hat{C}_D\lambda}{4(1-a_0)}\right)\varphi + \frac{\hat{C}_L a_c}{2(1-a_0)}, \tag{10a}$$

$$\frac{V_{Y_{\text{CyPC}}}}{U_0} = \frac{\hat{C}_L\lambda(2a_c/\lambda + \theta_c/2)}{2(1-a_0)}\cos(\gamma). \tag{10b}$$

For the CyPC case, both the term due to the cyclic pitching amplitude θ_c and to the cosine of the inflow a_c are small. Hence, this expression shows that CyPC, being unable to generate significant lateral forces and –consequently– velocities, results only in a small lateral displacement of the wake.

For the YM case, the lateral velocity is linearly proportional to the misalignment angle φ, and the term due to the cosine term of the axial inflow a_c is small. The coefficient of proportionality of the lateral velocity with respect to the misalignment angle is significant, and mostly due to axial induction (or, from a force point of view, from the presence of a lateral component of the thrust). This shows that YM is capable of effectively displacing the wake laterally, differently from CyPC.

2.2. Numerical model

To develop a higher fidelity model of the wake deflection problem, a computational fluid dynamic (CFD) tool is developed based on SOWFA [6]. The current version of the code uses an actuator line method embedded in a large eddy simulation (LES) environment, coupled with the aeroservolastic simulator FAST [12]. An immersed boundary (IB) formulation [10] is used to model the wind turbine nacelle and tower.

2.3. Experimental model

An experimental facility for the simulation of wind turbines and wind farms in a boundary layer wind tunnel [2] has been developed at the Wind Energy Institute of Technische Universität München (TUM). The real-time-controlled scaled wind turbine models enable experiments in aeroservoelasticity, the study of wakes, machine-to-machine interactions, and wind farm control for power maximization and load mitigation. In this work, one G2 wind turbine (Generic wind turbine, 2 m diameter) was tested in the boundary layer wind tunnel of the Politecnico di Milano, as shown in Fig. 3. The model was operated with both the YM and CyPC control strategies. The resulting effects were measured by scanning the wakes using triple hot wire probes, obtaining maps of the wake characteristics and position.
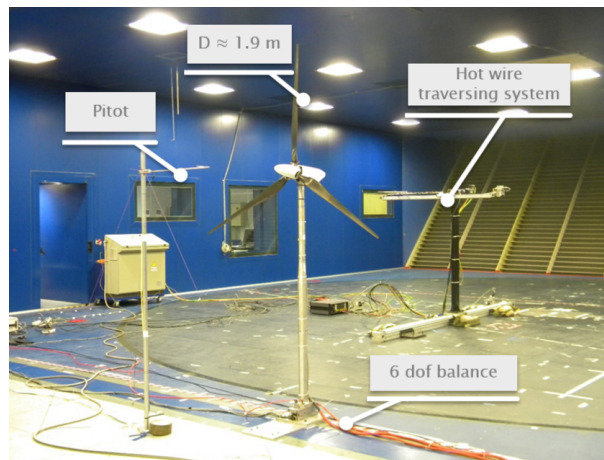
Figure 3: Scaled wind turbine and supporting measurement equipment in the wind tunnel of the Politecnico di Milano.

3. Results and analysis

3.1. Analytical model verification

We first compare the results of the analytical and simulation models, with the goal of supporting the insight on the YM and CyPC strategies offered by the analytical equations. To this end, the 5 MW NREL reference wind turbine [13] is used.

The main parameters appearing in the analytical model were calibrated using CFD simulations in uniform wind conditions, coupled with a FAST model where the elastic degrees of freedom had been switched off. The aerodynamic coefficients $C_{L\alpha}$ and C_D were obtained by extracting the corresponding values from the aeroelastic model. Both coefficients were averaged in the spanwise direction along the blades and in time over 10 rotor revolutions. The axial and swirl induction coefficients of Eqs. (2) were computed by first averaging the velocity at the rotor disk over 10 revolutions, and then computing U_P and U_T at 70% span at some different azimuthal positions. The unknown axial and swirl induction coefficients were finally computed by least-squares using Eqs. (1) collocated at these sampling azimuthal points.

The machine operates with a wind speed $U_0 = 8.2$ m/sec, an aerodynamic power of 2.31 MW, a power coefficient $C_P = 0.482$, a rotor speed of 9.81 RPM and a tip speed ratio TSR$= 8.1$, an operating condition where the strongest wake deficits are observed [7]. For the CyPC strategy the cyclic pitch amplitude is $\theta_c = 7$ deg with a phase $\gamma = 180$ deg, while for YM the misalignment angle is $\varphi = 20$ deg.

Table 1 shows the H in-plane force component computed by the analytical model and by CFD. Comparison of these figures shows a good agreement between the two models for both the CyPC and the YM strategies, with errors of 2.6% and 3.8%, respectively. Although the CyPC force is larger than the YM one, it should be noticed that in the CyPC case the rotor is aligned with the incoming wind; therefore, this is all the lateral force that the rotor is capable of exerting on the flow. On the other hand, for the YM case the thrust contributes a large lateral force (much larger than H), which in turn is responsible for causing a significant lateral wake displacement.

The same table also reports the nodding and yawing moments at the main bearing. It appears that the use of CyPC not only is unable to generate large lateral forces (which would be useful for deflecting the wake), but it also generates large nodding moments, as already noticed in Ref. [8]. Clearly, this is undesirable, because when the machine is subjected to gusts or enters into a shutdown from an overloaded condition, it will typically generate higher peak loads, which

Table 1: Comparison of analytical and CFD rotor in-plane force H (in kN), and CFD nodding and yawing moments (in kNm).

	Type	H	M_y	M_z
CyPC	Analytical	-3.01	-	-
θ_c=7 [deg]	Simulation	-2.93	4313.02	274.51
YM	Analytical	-2.10	-	-
φ=20 [deg]	Simulation	-2.18	-337.31	-211.18

in turn might become design drivers [3].

Table 2 shows the V_Y lateral velocity component computed by the analytical model and by CFD. For the CFD case, the table reports not only the velocity at the rotor disk (noted 0D in the table), but also at a few distances downstream of the wind turbine. Here again, although extremely simple, the analytical model appears to be capable of capturing the right order of magnitude of this velocity component. The table also clearly illustrates that, primarily thanks to the large lateral force obtained by tilting the thrust away from the incoming wind (responsible for the $a_0\varphi$ term in Eq. (10a)), the YM strategy attains significant lateral velocities at the rotor disk, while the CyPC strategy does not. This different lateral behavior of the wake is clearly noticeable also downstream from the rotor disk. For the CyPC case, the velocity is not only small but it also changes sign, indicating a more complex wake behavior that will be illustrated next.

Table 2: Comparison of analytical and CFD lateral velocities V_Y (in m/sec).

	Type	0D	1D	4D	7D	10D
CyPC	Analytical	0.03	-	-	-	-
θ_c=7 [deg]	Simulation	0.03	-0.03	0.05	0.02	0.03
YM	Analytical	0.29	-	-	-	-
φ=20 [deg]	Simulation	0.35	0.34	0.36	0.39	0.31

3.2. Wake behavior

The simple analysis of averaged wake properties as the lateral velocity and in-plane rotor force are clearly not sufficient for a complete understanding of the effects of YM and CyPC. Therefore, a more detailed characterization is attempted with the help of CFD.

Figure 4 shows the longitudinal instantaneous flow velocity magnitude $|\vec{u}|$ on a hub-height horizontal plane for the YM case with $\varphi = 20$ deg (left) and for CyPC using $\theta_c = 7$ deg $\gamma = 180$ deg (right). The plot on the left shows a marked wake deflection, in accordance with the analytical model. The wake has the typical expected symmetrical shape, and breaks down about 5D downstream from the rotor. On the other hand, the velocity plot for the CyPC case shows a drastically different behavior. First, there is little if none lateral movement. Furthermore, the velocity within the wake is far from symmetrical, revealing a region of significantly lower speed on one side of the rotor disk. This is caused by cyclic pitching that, by changing the azimuthal loading on the disk, creates a significant tilting of the axial induction plane. In turn, this effect generates a non-symmetrical warped downstream wake shape. The figure also shows that this

lack of symmetry generates a stronger mixing with the external flow than in the YM case, in turn leading to a faster wake recovery.
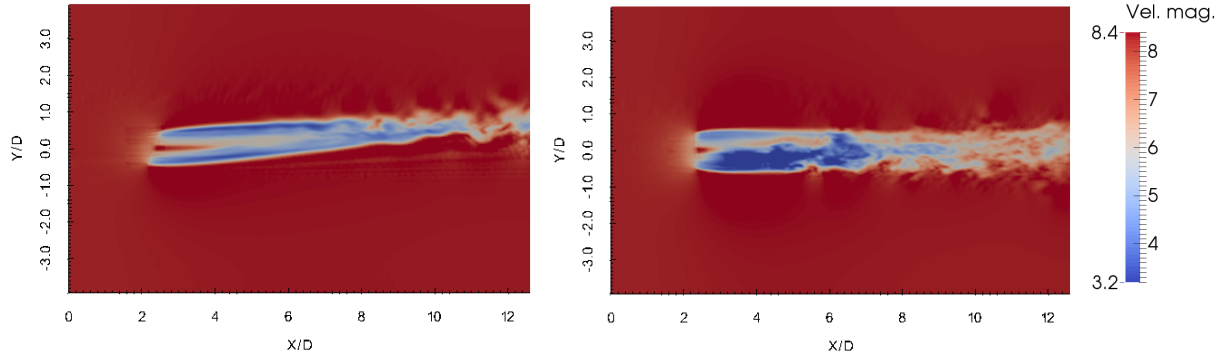

Figure 4: Velocity magnitude $|\vec{u}|$ for YM (left) and CyPC (right).

The Lambda$_2$ criterion [11] is used to better visualize the coherent vortical structures in the wake at hub height. For this purpose, the velocity gradient tensor $\mathbf{J}$ is decomposed into its symmetric $\mathbf{S}$ and antisymmetric $\mathbf{\Omega}$ parts. Then, the eigenvalues of $\mathbf{S}^2 + \mathbf{\Omega}^2$ are calculated and ordered in such a way that $\lambda_1 \geq \lambda_2 \geq \lambda_3$. A negative λ_2 indicates the presence of a vortex core [11]. For the CyPC case, reported on the right in Fig. 5, a concentration of vortical structures appears at 4D, on account of the wake breaking down and mixing with the external flow. The left part of the plot shows, on the other hand, a markedly more uniform behavior for the YM case.
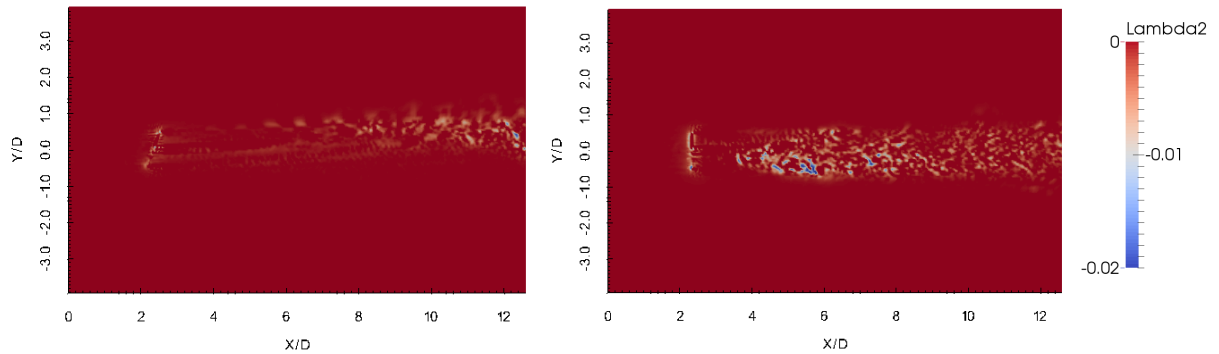

Figure 5: Lambda2 vortex criterion λ_2 for YM (left) and CyPC (right).

Figure 6 shows the instantaneous vorticity ω. Here again, the pictures highlight the drastically different behavior of the wakes in the two cases.

The wake geometry is further illustrated in Fig. 7, which reports the time-averaged longitudinal velocity component U_X in vertical planes at 1D, 3D, 5D and 7D downstream of the rotor disk. Here, the visualization shows the initial nearly axisymmetrical behavior of the wake for the YM case up to 3D. Significant lateral wake deflections can be observed from the plot. Further downstream, the wake structure is then deformed by its own lateral motion. For the CyPC case, the plot shows the effects of the tilting of the axial induction at 1D, which is largely responsible for the generation of large nodding moments on the rotor. This is followed by a tendency of the wake deficit to swirl during its downstream propagation, the average swirl rate from 0D to 7D being about 0.47 rad/D. After 6D, the angular momentum decays rapidly.
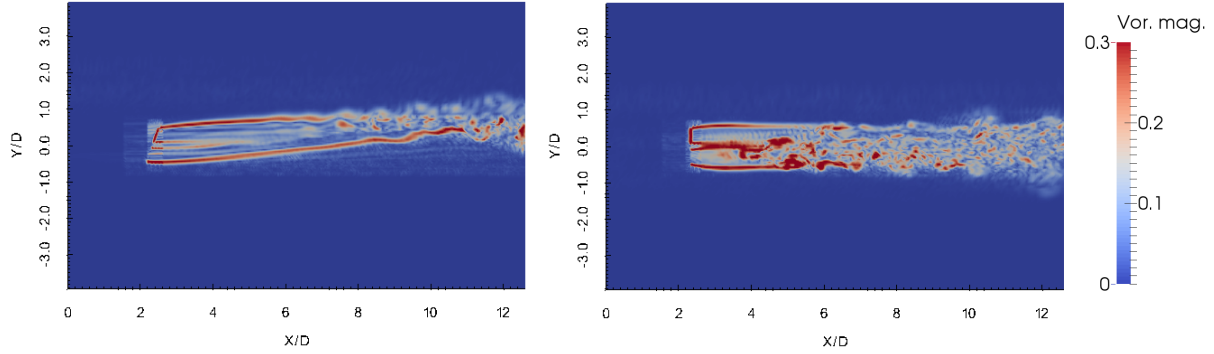
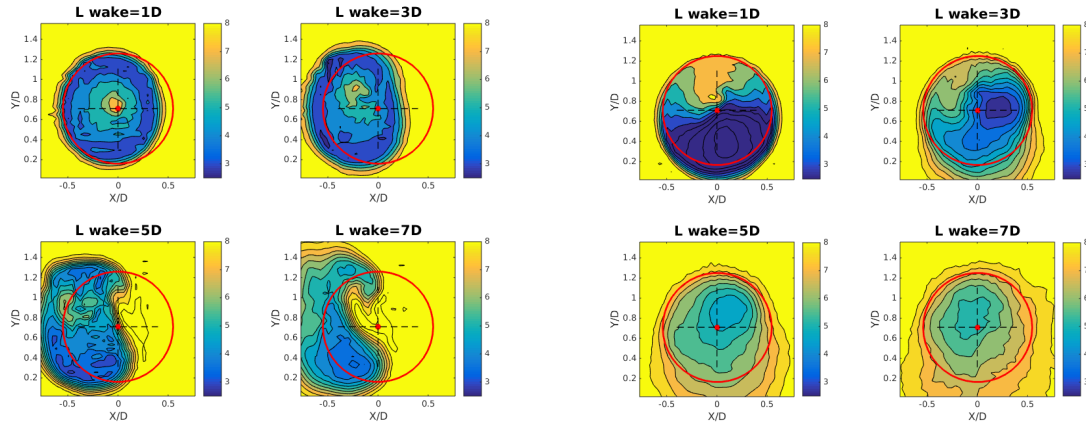Figure 6: Vorticity magnitude $|\vec{\omega}|$ for YM (left) and CyPC (right).

Figure 7: Longitudinal flow velocity U_X for YM (left) and CyPC (right).

3.3. Wake redirection

The wake redirection effectiveness of the two strategies is further verified by comparing the numerical simulations with experimental measurements.

Equations (10) indicate that only YM is capable of significantly deflecting a wake. In addition, Eq. (10a) points to the fact that wake displacement is, to a first order approximation, linearly dependent on the misalignment angle φ and on the average axial induction (which both should be nearly constant for all well designed rotors in the partial load region). Furthermore, the same displacement is only marginally dependent on the rotor design parameters and operating conditions. To help corroborate these conclusions, different rotors and operating conditions were used for the experimental and numerical simulations.

To correct for the minor effects highlighted by Eq. (10a) and due to TSR and design (through C_D and σ), the following adjustment procedure was devised. First, the wake lateral displacement is written by rearranging the previous expressions to get

$$\frac{l}{X} = (f - gC_D\lambda\sigma)\varphi, \tag{11}$$

where $f = Ca_0$ and $g = C(1+a_0')/(4(a-a_0))$. Then, by having measurements of l/X for various φ values, one may readily estimate by least-squares the coefficients f and g for both rotor S (simulation) and E (experiment). The measurements of one of the two (for example, E) can now

be adjusted as

$$\left(\frac{l}{X}\right)_{E \text{ adjusted}} = (f_E - g_E C_{D_E} \lambda_E \sigma_E K)\varphi_E, \tag{12}$$

where $K = (C_{D_S}\lambda_S\sigma_S)/(C_{D_E}\lambda_E\sigma_E)$.

The results are shown in Fig. 8, which reports wake displacements at a 4D distance downstream from the rotor. For YM (left), displacements are plotted as function of the misalignment angle φ, while for CyPC (right) as function of the cyclic pitch amplitude θ_c. CFD simulation results are plotted using triangles connected by blue lines, experimental results with $\times$ symbols connected by a red line, and finally experimental results adjusted according to Eq. (12) are shown with a yellow line.
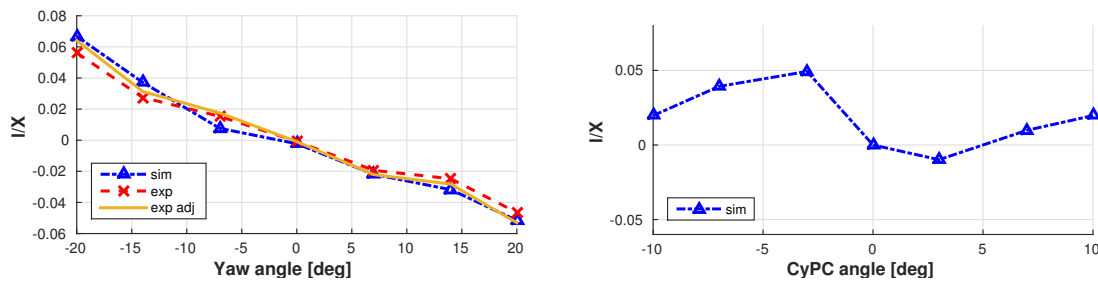

Figure 8: Wake displacement for YM vs. yaw misalignment φ (left), and for CyPC vs. cyclic pitch amplitude θ_c (right).

For the YM case, the curves show a roughly linear behavior of the wake center motion with the yaw angle, as predicted by the analytical model. The slopes for the uncorrected experiments and simulations are -0.039 and -0.034, respectively, which implies a close aerodynamic behavior of the two rotors. The effects of the adjustment to account for a different rotor design and operating conditions is also small, as expected. The rotor solidity σ is 0.052 for the 5 MW wind turbine used in the CFD simulations, and 0.047 for the experimental scaled model. The TSR λ is 8.1 for the simulation model and 7.5 for the experimental one. These results highlight the fact that non-dimensional wake displacement is, roughly, the same for different rotors operating in different conditions in the partial load regime.

Both experiments and simulations show that wake deflection is slightly non-symmetric with respect to the yaw direction on account of the effects of the spinning direction of the rotor, which breaks the symmetry of the problem. This effect is not directly captured by the simple analytical model of Eq. (10a), because a_c is assumed to be caused by φ, so that when the latter is zero the former should also be null.

The CyPC case is reported on the right part of Fig. 8. The plot shows an initial linear growth of displacement with cyclic pitch amplitude, which then rapidly saturates, possibly due to stall effects on the blades. The magnitude of the displacement appears to be comparable to the YM case, but this is misleading. In fact, the plot was generated by tracking the lateral position of the point in the wake characterized by the smallest longitudinal velocity, assumed by definition as the wake center. Looking at Fig. 7, it is clear that this point can undergo a significant lateral movement even for CyPC, because of the large warping of the wake shape caused by the tilting of the axial inflow plane. This however is not really accompanied by an effective lateral motion of the whole wake, as clearly illustrated by the graphical visualization of the flow field.

3.4. Power capture
The objective of wind farm control is to achieve an increased power capture for interacting wind turbines. The previous analyses have indicated that YM achieves significant lateral wake

displacement that, in principle, can be used for reducing the interaction of a wake with a downstream wind turbine. On the other hand, while CyPC is unable to laterally move the wake, it may produce a faster wake recovery that may result in an increased power capture on the downstream machine. Clearly, in all situations, these strategies will result in a net power increase only if what is gained on the downstream machine more than offsets what is lost on the front one.

A comprehensive analysis of this problem is clearly beyond the scope of the present work, and it would require simulating at least two interacting wind turbines in a wide range of relative positions, as well as atmospheric and operating conditions. Here we consider only a very limited set of conditions, to highlight the fact that even CyPC might occasionally lead to power capture gains.

The analysis is conducted in a simplified manner by simulating one single wind turbine. The power on a wind-aligned (full waked) downstream machine is estimated by averaging in space and time U_X on a rotor disk area at several different downstream distances (see red circle in Fig. 7). The power variation ΔP_{tot} for the two interacting wind turbines [9] is computed as

$$\Delta P_{\text{tot}}(X) = \Delta P_u + \frac{1}{2}\rho A \left(U_{X1}^3(X) - U_{X0}^3(X) \right) C_P, \tag{13}$$

where ΔP_u is the power loss/gain for the upstream machine, $C_P = 0.482$ the power coefficient of the 5 MW NREL wind turbine [13], U_{X1} the rotor-averaged mean longitudinal velocity for CyPC or YM as a function of downstream position X, and U_{X0} the same quantity for the baseline case without CyPC nor YM.

The rotor-averaged longitudinal velocity U_X is plotted vs. downstream distance on the left part of Fig. 9. The right part of the same figure plots the total power change given by Eq. (13). The CyPC cases are reported with circle ($\gamma = 0$ deg) and triangle ($\gamma = 180$ deg) symbols connected by blue lines, while the YM case by $\times$ symbols and a red line.
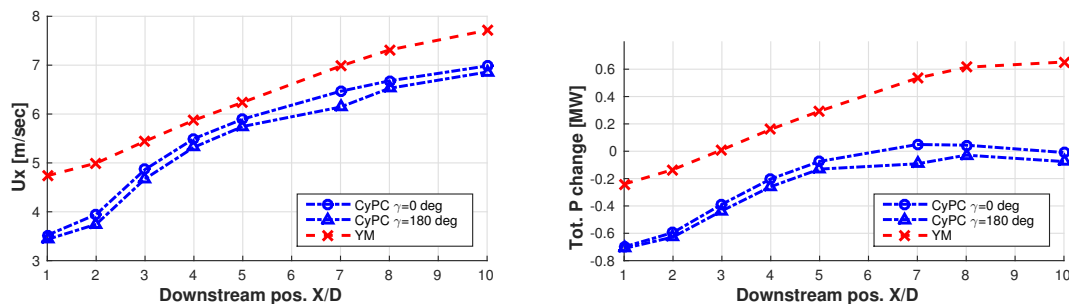

Figure 9: Downstream longitudinal flow velocity U_X (left) and total power change (right) vs. downstream position X/D for the CyPC and YM cases.

The plot shows that, even at this small interaction distance of 4D and in a fully aligned configuration, the wake displacement induced by YM is able to obtain significant increases in the average wind speed at the downstream wind turbine rotor disk. The yaw misalignment results in a net power gain starting from a downstream distance of 3D in this particular configuration. We have also demonstrated significant power gains in other operating conditions, and particular for partial wake overlaps [4, 5].

The same plots show a downstream speed increase in the near wake region for CyPC, due to the enhanced mixing of the wake. In turn, this leads to a total power capture recovery rate $\Delta P_{\text{tot}}/X \approx 0.13$ MW/D between 1D and 5D for both $\gamma = 0$ and 180 deg. At this distance the power loss on the front machine is compensated by the gain on the downstream one. Due to

the unsymmetrical behavior of the wake, wake recovery is slightly different for the $\gamma = 0$ and 180 deg case, which leads to a small total power gain for 0 deg and a slight power loss for 180 deg. Clearly, while a modest power increase is obtained by CyPC in this particular configuration and operating condition, this positive effect would have to be traded against a significant increase in the loading of the machine, as previously shown.

4. Conclusion and outlook

This paper has used a three-pronged approach to study wake redirection. A simplified analytical model was developed to gain some insight on the main parameters affecting this phenomenon. A CFD simulation model was used for a more refined representation of the complex dynamics of the fluid flow and its interaction with the wind turbine. Finally, scaled models where tested in a boundary layer wind tunnel, obtaining direct measurements of performance and operational parameters.

The main conclusions of this work are as follows. First, YM is more effective than CyPC in displacing the wake laterally, because it can generate significant lateral forces by tilting the thrust with respect to the incoming wind, in turn generating lateral components of the flow velocity. The amount of wake displacement is roughly linear with the misalignment angle (for small angles) and largely independent of design and operational parameters. In this sense, most rotors can be expected to produce similar non-dimensional wake displacements when yawed away from the wind. Third, CyPC, by tilting the axial inflow plane, generates high nodding moments on the machine but also a faster wake recovery due to enhanced mixing.

Work is progressing on multiple fronts. On the CFD side, we are simulating up to three interacting wind turbines and comparing the results with experimental observations conducted in the wind tunnel. The long term goal is to obtain a validated and calibrated simulation model of the whole experimental setup, capable of representing a variety of operating conditions of interest for wind farm control applications. On the experimental side, particle image velocimetry (PIV) is being used to understand the effects of CyPC on wake development and breakdown, supporting the CFD analyses shown here, while the closed-loop control capabilities of the models are being exploited for experimenting with wind farm control.

References

[1] R.L. Bisplinghoff and Holt Ashley. *Principles of aeroelasticity*. Courier Corporation, 2013.

[2] C.L. Bottasso, F. Campagnolo, and V. Petrović. Wind tunnel testing of scaled wind turbine models: Beyond aerodynamics. *Journal of Wind Engineering and Industrial Aerodynamics*, 127:11–28, 2014.

[3] C.L. Bottasso, A. Croce, CED Riboldi, and M. Salvetti. Cyclic pitch control for the reduction of ultimate loads on wind turbines. In *Journal of Physics: Conference Series*, volume 524, page 012063. IOP Publishing, 2014.

[4] F. Campagnolo, A. Croce, E.M. Manos, V. Petrović, J. Schreiber, and C.L. Bottasso. Wind tunnel testing of a. closed-loop wake deflection controller for wind farm power maximization. In *TORQUE 2016, The Science of Making Torque from Wind*. IOP Publishing, 2016.

[5] F. Campagnolo, V. Petrović, E.M. Manos, C.W. Tan, C.L. Bottasso, and I. Paek. Wind tunnel testing of power maximization control strategies applied to a. multi-turbine floating wind power platform. In *The 26th International Ocean and Polar Engineering Conference*. ISOPE, 2016.

[6] M. Churchfield and S. Lee. Nwtc design codes-sowfa. *URL: http://wind. nrel. gov/designcodes/simulator S./SOWFA*, 2012.

[7] M. Churchfield, S. Lee, P.J. Moriarty, Luis A. Martinez, Stefano Leonardi, Ganesh Vijayakumar, and J.G. Brasseur. A. large-eddy simulation of wind-plant aerodynamics. *AIAA paper*, 537:2012, 2012.

[8] P.A. Fleming, P.M.O. Gebraad, S. Lee, Jan-Willem van Wingerden, Kathryn Johnson, M. Churchfield, John Michalakes, Philippe Spalart, and Patrick Moriarty. Evaluating techniques for redirecting turbine wakes using sowfa. *Renewable Energy*, 70:211–218, 2014.

[9] P.M.O. Gebraad, F.W. Teeuwisse, J.W. Wingerden, P.A. Fleming, S..D. Ruben, J.R. Marden, and L.Y. Pao. Wind plant power optimization through yaw control using a. parametric model for wake effectsa. cfd simulation study. *Wind Energy*, 19(1):95–114, 2016.

[10] Hrvoje Jasak and Damir Rigler. Finite volume immersed boundary method for turbulent flow simulations. In *9th OpenFOAM Workshop*, 2014.

[11] Ming Jiang, Raghu Machiraju, and David Thompson. Detection and visualization of. *The Visualization Handbook*, page 295, 2005.

[12] J.M. Jonkman and Marshall L.B. Buhl. Fast users. guide nrel. Technical report, EL-500-29798, National Renewable Energy Laboratory, Golden, CO, 2004.

[13] J.M. Jonkman, Sandy Butterfield, Walter Musial, and George Scott. Definition of a. 5-mw reference wind turbine for offshore system development, 2009.

[14] J.F. Manwell, J.G. McGowan, and A.L. Rogers. *Wind energy explained: theory, design and application.* John Wiley & Sons, 2010.